Optics Letters

Experimental performance of deep learning channel estimation for an X-ray communication-based OFDM-PWM system

Wenxuan Chen,[1,2] Yunpeng Liu,[1,2,*] Junxu Mu,[1] Zhaopeng Feng,[1] and Xiaobin Tang[1,2]

[1]Department of Nuclear Science and Technology, Nanjing University of Aeronautics and Astronautics, Nanjing 210016, China
[2]Key Laboratory of Nuclear Technology Application and Radiation Protection in Astronautics, Ministry of Industry and Information Technology, Nanjing 210016, China
*Corresponding author: liuyp@nuaa.edu.cn

Received 16 September 2021; revised 4 December 2021; accepted 8 December 2021; posted 9 December 2021; published 16 January 2022

A deep learning channel estimation scheme in orthogonal frequency division multiplexing for X-ray communication (XCOM) is studied. The scheme uses simulated and detected data obtained with different working parameters and numbers of pilots as training and testing data, respectively, for the deep neural network (DNN) model. The bit-error-rate performance of the DNN model under various system operating parameters, numbers of pilot sequences, and channel obstructions is investigated separately. Experiment results showed that the deep-learning-based approach can address the distortion of the air-scintillator channel for XCOM, giving a performance comparable to those of least-squares and minimum-mean-square error estimation methods.

https://doi.org/10.1364/OL.443128

X-ray communication (XCOM) is a type of wireless optical communication technology that uses a modulated X-ray beam as carrier for data transmission. XCOM is characterized by high X-ray photon energy and strong penetrability, and is regarded as an effective method for solving the issue of communication shielding in communication blackouts [1–3]. Radio interference in space has become increasingly complicated with the increasing number of space exploration missions, and electromagnetic interference has become a hidden danger that must be considered [4–6]. X rays can be protected from electromagnetic interference from other communication links during transmission [7]. X rays need to pass through the cabin shell, high-temperature plasma, thin atmosphere, and other channels after emission from the launching end during the landing of the spacecraft [8–10].Due to the attenuation of x rays in the air and the uncertainty in X-ray energy deposition by scintillators, traditional channel estimation methods deteriorate. Hang *et al*. [7] demonstrated that the stability of XCOM in the dusty environment of Mars is better than that of an optical link. Wang *et al*. [11] showed that bit error rates (BERs) of on–off keying (OOK) and pulse position modulation (PPM) are approximately at the 10^{-4} level with a communication rate of 25 kbps. Our previous work investigated orthogonal frequency division multiplexing combined with pulse width modulation (OFDM-PWM) in XCOM, and 360 kbps under 3.8×10^{-3} was achieved in the experiment [12]. Moreover, orthogonal frequency division multiplexing (OFDM), which has been successfully applied in visible light communication (VLC) systems [13–17], is also used in the XCOM system due to its resistance to inter-symbol interference (ISI) in the complex channel. Redundant signals, such as pilots in the traditional channel estimation scheme, further occupy spectrum resources. Traditional estimation approaches, such as least-squares (LS) and minimum-mean-square error (MMSE) methods, have also been utilized in various conditions [18]. The LS method is simple and easy to implement but sensitive to external noise. The MMSE method can successfully address selectivity in both frequency and time for a fading channel. Among various solutions to the channel estimation of signals in optical communication, several machine learning (ML) techniques have already shown their high potential to improve system performance [19–22]. Because the air-scintillator channel in XCOM is a time-varying channel, pilots are generally used for channel estimation, and a deep neural network (DNN) can capture the potential characteristics of channel changes and predict the channel well based on the pilot sequence in XCOM due to its own good predictive ability.

An XCOM channel estimation based on the DNN model is proposed in this Letter. The XCOM channel is mainly assumed to be the air-scintillator channel because previous studies have shown that X-rays can penetrate a plasma channel almost without attenuation. Training data is composed of simulation data and air-scintillator channel impulse response, and experimental data are regarded as testing data. The results verify that the DNN model can learn and distinguish the characteristics of the XCOM air-scintillator channel. This study pioneers the application of channel estimation based on a deep learning method to XCOM. The experimental results show that the utilization of deep learning models can achieve better performance than traditional methods when sufficient pilots exist in the OFDM-PWM system. Signals with various channel characteristics are collected by adjusting different system working parameters, such as the filament current, grid voltage, anode voltage, and distance between the receiver and transmitter. Deep learning methods can achieve a data rate of 1.14 Mbps under the existing experimental conditions at a BER of 9.13×10^{-4}.

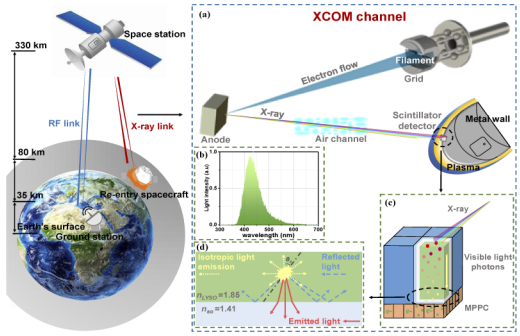

Fig. 1. XCOM system link: (a) XCOM channel model in the communication blackout, (b) LYSO scintillator excitation spectrum, (c) diagram of the scintillator detector, and (d) total reflection of isotropic photons at the surface between the optical coupling agent and scintillator.

A communication blackout generally occurs at a height of 35–80 km above the ground, as shown in Fig. 1. X rays generated by electron bombardment of an anode target need to pass through a channel, such as the thin atmosphere, plasma, or scintillator, as shown in Fig. 1(a). Due to the high energies of X-rays, a lutetium–yttrium oxyorthosilicate (LYSO) scintillator detector is used as the receiver. X rays can deposit energy in the scintillator and generate visible light that can be detected by the photodetector. X rays demonstrate different attenuation coefficients in air and various light yields in the scintillator because the x rays emitted by an X-ray tube have a spread of energies, as shown in Fig. 1(b). Approximately 30% of the photons are lost due to the self-absorption effect of the LYSO scintillator on visible photons generated by X-ray deposition. Moreover, X-ray photons of different energies deposit their energies at varying positions in the scintillator, as shown in Fig. 1(c). Visible light photons generated at different positions reach the scintillator at varying angles, leading to different probabilities of total reflection for different photons. A large number of isotropic visible light photons are totally reflected at the exit surface; less than 20% of the photons will be emitted from the exit surface and detected by multipixel photon counters (MPPCs) due to the high refractive index of the LYSO scintillator, which has a refractive index n_{LYSO} of 1.85 and a critical angle of $\theta_c = \sin^{-1}(n_{so}/n_{LYSO})$, as shown in Fig. 1(d) [23]. This complex channel presents challenges to channel estimation.

A block diagram of our proposed scheme tested here is illustrated in Fig. 2. First, multilevel quadrature amplitude modulation (M-QAM) is used to modulate N = 64 subcarriers. A real OFDM signal is generated by constraining the complex vector

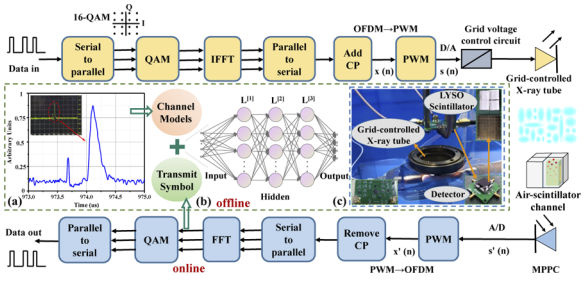

Fig. 2. System model of XCOM using the DNN model: (a) air-scintillator channel impulse response, (b) DNN model, and (c) diagram of the experimental platform.

of the input to the inverse fast Fourier transform (IFFT), enforcing Hermitian symmetry. Second, OFDM signals are loaded into an arbitrary waveform generator (RIGOL DG5102), and the voltage of the output signal is 0–5 V. The electric field distribution in front of the cathode can be changed by using the generated OFDM-PWM signal to adjust the grid potential and control the number of electrons bombarding the anode target. Then, the intensity of the emitted x ray is changed to realize X-ray modulation. Third, the detector, which is composed of a 2×2 array of LYSO scintillators (10 × 10 × 5 mm) and an 8×8 array of MPPCs (3 × 3 mm), collects X-ray signals. Finally, the detected electrical signals are digitized and stored using a real-time oscilloscope (Keysight DSOS054A) at a sampling rate of 100 MSa/s.

These photons are detected by MPPCs (Hamamatsu S13360-3050VE, bandwidth > 200 MHz) after multiple reflections inside the scintillator. As shown in Fig. 2(a), the radioactive source ^{241}Am, which has a similar energy to the X-ray energy of the system, is utilized to describe the air-scintillator channel model in the XCOM and measure the impulse response of the LYSO scintillator. In order to increase the randomness of the channel in the simulation, we measured and sampled ^{241}Am single-photon pulses at different distances as the atmospheric-scintillator channel impulse response. Energy deposition occurs in the scintillator when the high-energy photon is incident on the LYSO scintillator, and a large number of isotropic visible light photons (approximately 25,000 photons/MeV) with a peak wavelength of 420 nm are generated at a certain depth because radioactive sources can generate a single photon. The impulse response of the air-scintillator channel can be obtained by recording the arrival times of different photons in the MPPC detector.

An X-ray channel impulse response model was studied [12]. A sample-spaced air-scintillator multipath channel $h(t)$ is described using the channel impulse response of the LYSO scintillator. The received signal can be expressed as

$$y(t) = x(t) \otimes h(t) + n(t), \tag{1}$$

where $\otimes$ denotes the circular convolution and $x(t)$ and $n(t)$ represent transmitted data and additive white Gaussian noise (AWGN), respectively.

As shown in Fig. 2, offline training and online testing are included to achieve an effective DNN model for XCOM channel estimation. The model is trained with received OFDM samples that are generated with various data and under air-scintillator channel conditions through simulation in the offline training stage. The received frequency-domain signal after performing FFT is expressed as follows:

$$Y(n) = H(n)X(n) + N(n). \tag{2}$$

The structure of the DNN model with 256, 600, 300, 150, 8 neurons in its layers is shown in Fig. 2(b). Simulated data after FFT and the air-scintillator channel impulse response are regarded as the training data for the DNN model. The input of the deep learning model is the received data for the pilot block and one data block. Every eight bits of transmitted data are grouped on the basis of a single model trained independently in the output layer and then concatenated in series to generate 256 bits of output data. Experimental data are regarded as the testing data for the DNN model. In order to ensure good generalization ability of the network during the training process, the number of

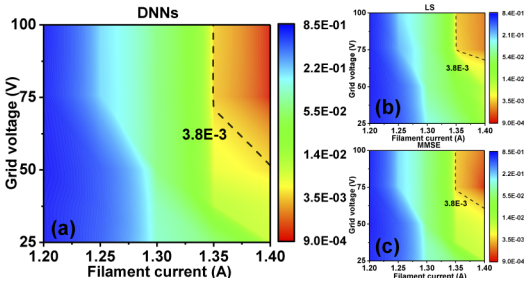

Fig. 3. BER for different filament currents and grid voltages, as obtained with (a) DNNs, (b) LS, and (c) MMSE (transmission distance = 0.15 m, anode voltage = 30 kV, and pilot = 16).

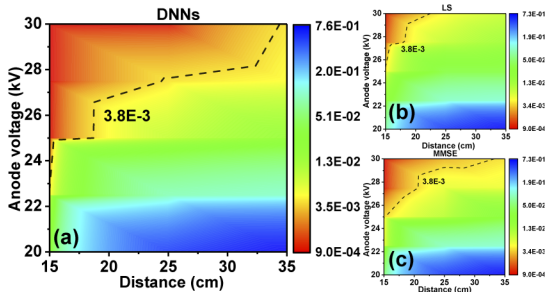

Fig. 4. BER for different anode voltages and distances between the receiver and transmitter, as obtained with (a) DNNs, (b) LS, and (c) MMSE (filament current = 1.4 A, grid voltage = 65 V, and pilot = 16).

training sets selected in the experiment is 1×10^7 and the number of test sets is 3.3×10^6. During the training process, the loss function is less than 0.001 and considered to be convergent when it declines. The experimental platform is shown in Fig. 2(c).

Experimental data collected by the oscilloscope in the online stage are used to test the DNN model, which can recover transmitted data. The following cross-entropy function was chosen to act as the loss function in our experiment:

$$E = -\{\widehat{X}(n)\log[X(n)] + [1-\widehat{X}(n)]\log[1-X(n)]\}, \quad (3)$$

where $\hat{X}(n)$ and $X(n)$ are prediction and supervision symbols, respectively.

Signals from the system are collected under various operating parameters, such as different distances between transceiver terminals, anode voltages, filament currents, and grid voltages, to verify the performance and generalization ability of the DNN model in the experiment and explore a wide parameter space. These signals are used as the validation set for the DNN model.

The signal sampled at the receiving end passes through the LS, MMSE, and DNN channel estimation modules respectively. The result of the LS channel estimation is used as the autocorrelation matrix in the MMSE in the experiment. Figure 3 shows a performance comparison of the DNN, LS, and MMSE methods when the system was used under different filament currents and grid voltages. The number of emitted X-ray photons increased as the filament current increases, thereby reducing the BER of the system. Moreover, the grid electric potential fails to cut off the X-ray emission completely when the grid voltage is lower than 65 V, which results in low-level oscillations of the X-ray signals at the receiver. The low-level oscillations of the detected X-ray signals are small when the grid voltage of the system exceeds 65 V, and the BER of the system fails to decrease as the grid voltage increases because the grid potential can cut off the electron beam emitted by the filament. The LS method provides the worst performance given the absence of a prior statistic for the channel during the detection, while the DNN method presents better robustness to oscillations of the signals at the receiver.

Depending on the application scenario, there are many options for the energy of the emitted x ray in a real XCOM system. Hence, the performance of the DNN method was explored at different anode voltages and distances between the receiver and transmitter. As shown in Fig. 4, a low anode voltage and a long distance cause a high attenuation coefficient in the air-scintillator channel. The background voltage signal exceeds the high-level voltage of the X-ray signals when the distance between the receiver and transmitter is 0.18 m because the LYSO array scintillator presents high background radiation. The BER of the system can only be reduced by increasing the anode voltage.

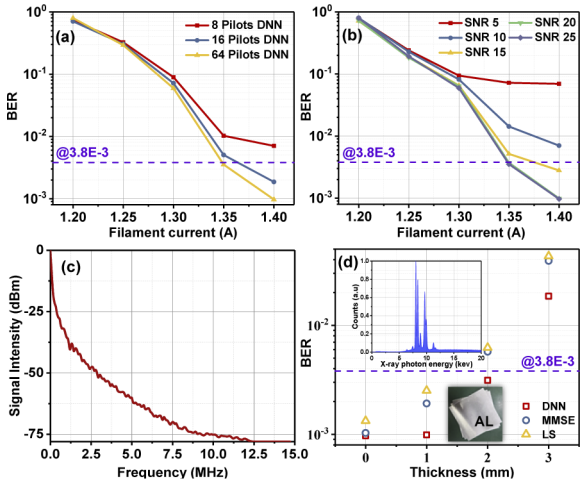

Fig. 5. (a) BER performance versus filament current for the DNN model with different pilots (8, 16, and 64) (transmission distance = 0.15 m, anode voltage = 30 kV, and grid voltage = 65 V). (b) BER performance versus filament current for different SNR of the training data for the DNN model (pilot = 64). (c) Bandwidth of the grid-controlled X-ray tube in the XCOM system, as measured with a logic analyzer. (d) BER performance versus thickness of the aluminum sheets placed in the path of the XCOM system with 64 pilots (inset shows the X-ray energy spectrum).

The DNN method provides higher accuracy than the LS and MMSE methods under more severe working conditions.

The experimental performance of each of the three channel estimation methods was tested when the pilot sequence was 8, 16, or 64 to improve the spectrum efficiency of the system. High spectrum utilization can be estimated with just a few pilots. Figure 5(a) shows the BER of the system under different filament currents when the number of pilot frequencies is 8, 16, or 64. The BER is below 3.8×10^{-3} when 16 and 64 pilots are used and the filament current is 1.35 or 1.36 A, which proves that DNNs have the ability to remember and analyze the complicated characteristics of the air-scintillator channels when the number of pilots is small. According to the equivalent calculation of atmospheric density at different altitudes, the transmission distance is equivalent to 58–80 km under the communication blackout when the transceiver end is 0.35 m under the normal air channel based on calculations performed using the Monte Carlo N-Particle Transport Code System (MCNP) [24].

The DNN model was trained using different SNR data generated by simulation in order to verify the generalization ability of the network, and experimental signals with various filament currents were used to test different models and compare their BER performance, as shown in Fig. 5(b). The SNR of the training signals exceeded 15 dB, and the performance of the DNN model was lower than 3.8×10^{-3} when the filament current was 1.4 A. Figure 5(c) shows that the bandwidth of the grid-controlled X-ray tube was measured at a distance of 0.15 m to observe the trend in the signal-intensity decay with increasing frequency.

The influence of the metal wall on channel estimation is ignored in these results. The x ray shows satisfactory penetrating ability in the XCOM, but its energy spectrum changes to a certain extent after passing through the metal wall. Aluminum sheets of different thicknesses were placed along the ray's propagation path to test the effect of the DNN model in a metal shield channel. Figure 5(d) shows that the DNN-based model still provides improved results when metal walls of different thicknesses are added to the channel. The reason for the better performance of the DNN is that the characteristics of the metal shield channels can be learned based on the training data generated from the model.

A method for DNN-based channel estimation of the air-scintillator in the XCOM system is proposed in this Letter. For the first time to the best of our knowledge, we used the single-photon pulse measured by the scintillator to determine the air-scintillator channel impulse response. We realized a data rate of 1.14 Mbps and a BER of 9.13×10^{-4} with the OFDM-PWM modulation scheme when the system was operated with a transmission distance of 0.3 m, a filament current of 1.4 A, and an anode voltage of 30 kV. Additionally, the filament current, grid voltage, anode voltage, and distance between the receiver and transmitter were considered during channel estimation. The experimental results show that the performance of the DNN method compares favorably with those of the MMSE and LS methods using the same modulation scheme.

Funding. Chinese Aeronautical Establishment (2018ZC52029); Foundation of the Graduate Innovation Center, Nanjing University of Aeronautics and Astronautics (kfjj20200609); Fundamental Research Funds for the Central Universities.

Disclosures. The authors declare no conflicts of interest.

Data availability. Data underlying the results presented in this Letter are not publicly available at this time but may be obtained from the authors upon reasonable request.

REFERENCES

1. H. Li, X. Tang, S. Hang, Y. Liu, J. Mu, and W. Zhou, Phys. Plasmas **26**, 033503 (2019).
2. H. Li, X. Tang, S. Hang, Y. Liu, and D. Chen, J. Appl. Phys. **121**, 123101 (2017).
3. Y. Li, T. Su, L. Sheng, N. Xu, and B. Zhao, Mod. Phys. Lett. B **34**, 2050057 (2020).
4. J. A. Robinson, T. L. Thumm, and D. A. Thomas, Acta Astronaut. **61**, 176 (2007).
5. A. Riddle, RF Microw. Handb. RF Microw. Appl. Syst. **32**, 23-1 (2018).
6. P. Ehrenfreund, C. McKay, J. D. Rummel, B. H. Foing, C. R. Neal, T. Masson-Zwaan, M. Ansdell, N. Peter, J. Zarnecki, S. MacKwell, M. A. Perino, L. Billings, J. Mankins, and M. Race, Adv. Sp. Res. **49**, 2 (2012).
7. S. Hang, X. Tang, H. Li, Y. Liu, J. Mu, W. Zhou, P. Dang, and S. Lai, Acta Astronaut. **166**, 277 (2020).
8. J. E. Pavlosky and L. G. St. Leger, "Apollo experience report: thermal protection subsystem," NASA-TN-D-7564 (NASA, 1974).
9. I. F. Belov, V. Y. Borovoy, V. A. Gorelov, A. Y. Kireev, A. S. Korolev, and E. A. Stepanov, J Spacecr Rockets **38**, 249 (2001).
10. D. E. Mather, J. M. Pasqual, J. P. Sillence, and P. Lewis, *AIAA/CIRA 13th International Space Planes and Hypersonics Systems and Technologies Conference*, Capua, Italy, 19May2005, paper 2129.
11. L. Q. Wang, T. Su, B. S. Zhao, L. Z. Sheng, Y. A. Liu, and D. Liu, Acta Phys. Sin. **64**, 120701 (2015).
12. W. Chen, Y. Liu, X. Tang, J. Mu, and S. Lai, Opt. Express **29**, 3596 (2021).
13. P. Guan, K. M. Roge, H. C. H. Mulvad, M. Galili, H. Hu, M. Lillieholm, T. Morioka, and L. K. Oxenlowe, J. Lightwave Technol. **34**, 626 (2016).
14. Y.-C. Chi, D.-H. Hsieh, C.-T. Tsai, H.-Y. Chen, H.-C. Kuo, and G.-R. Lin, Opt. Express **23**, 13051 (2015).
15. H. M. Oubei, J. R. Duran, B. Janjua, H.-Y. Wang, C.-T. Tsai, Y.-C. Chi, T. K. Ng, H.-C. Kuo, J.-H. He, M.-S. Alouini, G.-R. Lin, and B. S. Ooi, Opt. Express **23**, 23302 (2015).
16. Y. Zhao, A. Wang, L. Zhu, W. Lv, J. Xu, S. Li, and J. Wang, Opt. Lett. **42**, 4699 (2017).
17. J. Xu, M. Kong, A. Lin, Y. Song, J. Han, Z. Xu, B. Wu, S. Gao, and N. Deng, Opt. Lett. **42**, 1664 (2017).
18. Y. S. Hussein, M. Y. Alias, and A. A. Abdulkafi, in *2016 IEEE 12th International Colloquium on Signal Processing and Its Applications, CSPA* (2016), pp. 204–209.
19. H. Ye, G. Y. Li, and B. H. Juang, IEEE Wireless Commun. Lett. **7**, 114 (2018).
20. H. Lu, M. Jiang, and J. Cheng, IEEE Trans. Commun. **69**, 2290 (2021).
21. Y. Zhao, P. Zou, W. Yu, and N. Chi, Opt. Express **27**, 22532 (2019).
22. M. A. Jarajreh, E. Giacoumidis, I. Aldaya, S. T. Le, A. Tsokanos, Z. Ghassemlooy, and N. J. Doran, IEEE Photonics Technol. Lett. **27**, 387 (2015).
23. A. Knapitsch, E. Auffray, C. W. Fabjan, J. L. Leclercq, P. Lecoq, X. Letartre, and C. Seassal, Nucl. Instruments Methods Phys. Res. Sect. A Accel. Spectrometers, Detect. Assoc. Equip. **628**, 385 (2011).
24. Tim Goorley, "Monte Carlo N-Particle transport code system including MCNP6. 1, MCNP5-1.60, MCNPX-2.7. 0 and data libraries," No. MCNP6. 1/MCNP5/MCNPX-EXE; 004380MLTPL00 (Los Alamos National Laboratory, 2013).